Early functional connectivity deficits and progressive microstructural alterations in the TgF344-AD rat model of Alzheimer's Disease: A longitudinal MRI study

Cynthia Anckaerts, Ines Blockx, Priska Summer, Johanna Michael, Julie Hamaide, Christina Kreutzer, Hervé Boutin, Sébastien Couillard-Després, Marleen Verhoye, Annemie van der Linden

Neurobiology of Disease 124 (2019) 93–107

Contents lists available at ScienceDirect

Neurobiology of Disease

journal homepage: www.elsevier.com/locate/ynbdi

Early functional connectivity deficits and progressive microstructural alterations in the TgF344-AD rat model of Alzheimer's Disease: A longitudinal MRI study

Cynthia Anckaerts[a,*], Ines Blockx[a], Priska Summer[b], Johanna Michael[b,c], Julie Hamaide[a], Christina Kreutzer[b], Hervé Boutin[d], Sébastien Couillard-Després[b], Marleen Verhoye[a], Annemie Van der Linden[a]

[a] Bio-Imaging Lab, University of Antwerp, Universiteitsplein 1, Wilrijk, Antwerp 2610, Belgium
[b] Institute of Experimental Neuroregeneration; Spinal Cord Injury and Tissue Regeneration Centre Salzburg, Paracelsus Medical University, Strubergasse 22, Salzburg 5020, Austria
[c] Institute of Molecular Regenerative Medicine; Spinal Cord Injury and Tissue Regeneration Centre Salzburg, Paracelsus Medical University, Strubergasse 22, Salzburg 5020, Austria
[d] Wolfson Molecular Imaging Centre, Faculty of Biology, Medicine and Health, Manchester Academic Health Sciences Centre, University of Manchester, Manchester M20 3LJ, UK

ARTICLE INFO

Keywords:
Alzheimer's disease
TgF344-AD
Resting state fMRI
rsfMRI
Diffusion tensor imaging
DTI
Functional connectivity
FC
Amyloid plaque

ABSTRACT

The development and characterization of new improved animal models is pivotal in Alzheimer's Disease (AD) research, since valid models enable the identification of early pathological processes, which are often not accessible in patients, as well as subsequent target discovery and evaluation. The TgF344-AD rat model of AD, bearing mutant human amyloid precursor protein (APPswe) and Presenilin 1 (PSEN1ΔE9) genes, has been described to manifest the full spectrum of AD pathology similar to human AD, *i.e.* progressive cerebral amyloidosis, tauopathy, neuronal loss and age-dependent cognitive decline. Here, AD-related pathology in female TgF344-AD rats was examined longitudinally between 6 and 18 months by means of complementary translational MRI techniques: resting state functional MRI (rsfMRI) to evaluate functional connectivity (FC) and diffusion tensor imaging (DTI) to assess the microstructural integrity. Additionally, an evaluation of macroscopic changes (3D anatomical MRI) and an image-guided validation of *ex vivo* pathology were performed. We identified slightly decreased FC at 6 months followed by severe and widespread hypoconnectivity at 10 months of age as the earliest detectable pathological MRI hallmark. This initial effect was followed by age-dependent progressive microstructural deficits in parallel with age-dependent *ex vivo* AD pathology, without signs of macroscopic alterations such as hippocampal atrophy.

This longitudinal MRI study in the TgF344-AD rat model of AD revealed early rsfMRI and DTI abnormalities as seen in human AD patients. The characterization of AD pathology in this rat model using non-invasive MRI techniques further highlights the translational value of this model, as well as its use for potential treatment evaluation.

1. Introduction

Alzheimer's disease (AD) is the most common cause of dementia and one of the most important causes of morbidity among the aging population. Since one of the hallmarks of AD is extracellular accumulation of amyloid β (Aβ) peptides, this has been a common and popular target for the development of transgenic mouse models of AD. The use of these transgenic mouse models has led to new insights in relation to the so-called "amyloid cascade hypothesis" (Barage and Sonawane, 2015; Hardy and Higgins, 1992). Although transgenic mouse models have been proven highly valuable in elucidating several pathological mechanisms involved in AD, they do not demonstrate robust Aβ plaque deposition in combination with distinct tauopathy and neuronal loss unless additional human transgenes are included, *e.g.* triple transgenic AD mouse model (Do Carmo and Cuello, 2013). Because rats are physiologically, genetically and morphologically closer to humans, they

* Corresponding author.
E-mail address: cynthia.anckaerts@uantwerpen.be (C. Anckaerts).

https://doi.org/10.1016/j.nbd.2018.11.010
Received 5 April 2018; Received in revised form 5 November 2018; Accepted 12 November 2018
Available online 13 November 2018
0969-9961/

offer numerous advantages compared to mice (Gibbs et al., 2004; Jacob and Kwitek, 2002). Cohen and colleagues developed a new transgenic rat model of AD, the TgF344-AD rat model, bearing mutant human amyloid precursor protein (APP_{swe}) and Presenilin 1 (PSEN1ΔE9) genes (Cohen et al., 2013). According to this initial publication, TgF344-AD rats demonstrate strong age-dependent amyloidosis as well as tauopathy and apoptotic loss of neurons, coincident with progressive cognitive decline between 6 and 26 months of age. Further research has shown that already at 4 months of age, this rat model shows enhanced anxiety-like behaviour (Pentkowski et al., 2018). As early as 6 months of age, the TgF344-AD rat model presents reduced basal synaptic transmission in entorhinal-hippocampal synapses. An effect which is followed by dysfunction of hippocampal CA3-CA1 synapses at 9 months in males and only at 12 months in females (Smith and McMahon, 2018). At 9 months of age, also neurovascular dysfunction has been observed using two-photon microscopy and electrophysiological measures (Bazzigaluppi et al., 2018; Joo et al., 2017). Another study described evidence of early tau accumulation and progressive dysfunction of the noradrenergic system in this rat model between 6 and 16 months of age (Rorabaugh et al., 2017). Interestingly, it has been shown that targeting noradrenergic dysfunction improves performance in the Morris Water maze in 16 month old animals (Rorabaugh et al., 2017) and that treatment aimed at preserving neuronal survival prevents depressive-like behaviour at 16 months as well as cognitive deficits at 24 months (Voorhees et al., 2017). In contrast to other rodent models with merely a single pathological aspect of AD (*e.g.* amyloidosis), this rat model is currently recognized as a highly clinically relevant model as it entails AD-related pathology much akin to the spatiotemporal pattern of human AD pathology (Braak and Braak, 1991; Braak and Braak, 1995; Thal et al., 2002).

Today, not only cerebrospinal fluid (CSF) biomarkers, but also neuroimaging techniques such as positron emission tomography (PET) and magnetic resonance imaging (MRI) have acquired a central position in ascertaining the diagnosis of AD, providing insights into the effects of AD pathology and its temporal and spatial evolution (Johnson et al., 2012). Structural and functional magnetic resonance imaging studies have gained immensely in popularity in the study of early events of AD. As such, structural MRI is used for the detection of atrophy due to dendritic and neuronal loss in brain regions such as the entorhinal cortex, hippocampus and posterior cingulate cortex (Dubois et al., 2007; Johnson et al., 2012). Beside macroscopic volume loss, microstructural changes can also be observed using diffusion tensor imaging (DTI) starting at earlier stages of the disease (Nir et al., 2013; Weston et al., 2015). Ever since the work of Brun and Englund in 1986, it is known that microscopic white matter changes are present in AD (Brun and Englund, 1986; Gold et al., 2012). Although many studies focus on white matter, grey matter changes also exist in early stages of AD in several brain regions, including the hippocampus, posterior cingulate cortex and subcortical regions, preceding macrostructural atrophy (Weston et al., 2015). Next to the observation of alterations in microstructural integrity in AD, markers of neuronal function have been shown to be useful in detecting AD-related pathology (Balachandar et al., 2015; Hoozemans et al., 2006) as the earliest pathological alterations include the presence of soluble Aβ and inflammation leading to synaptic deficits (Busche et al., 2012; Ewers et al., 2011; Rao et al., 2012; Selkoe, 2002; Shankar et al., 2007). For this, resting state functional MRI (rsfMRI) has been proven to be a valuable technique by allowing the observation of functional connectivity (FC) based on the blood oxygenation level dependent (BOLD) signal. FC refers to networks of spatially distributed, but functionally connected brain regions and is considered as an indirect measure of trans-synaptic activity (van den Heuvel and Hulshoff Pol, 2010). As such, altered FC has been observed in brain regions important for learning and memory, even before appreciable plaque deposition and the onset of clinical symptoms (Balachandar et al., 2015; Chase, 2014; Sheline and Raichle, 2013).

Within the present study, we aimed to longitudinally examine the transgenic TgF344-AD rat model of AD using these complementary non-invasive MRI tools, in order to enable future preclinical and translational AD research. More specifically, we studied i) functional connectivity using rsfMRI, ii) white and grey matter integrity using DTI, and iii) macrostructural changes using 3D anatomical MRI. Because AD is more common in women, female TF344-AD rats were selected and studied longitudinally between 6 and 18 months of age, *i.e.* from early stages up to more advanced stages of the disease. We hypothesized that the early pathological processes in AD that lead to synaptic deficits could be reflected by aberrant FC measured by rsfMRI. Additionally, we hypothesized that minor (early-stage) and major (late-stage) structural changes could be detected using DTI prior to macroscopic alterations. Lastly, we included *ex vivo* examinations to validate the underlying AD pathology.

2. Material & methods

2.1. Ethical statement

All procedures were performed in strict accordance with the European Directive 2010/63/EU on the protection of animals used for scientific purposes. The protocols were approved by the Committee on Animal Care and Use at the University of Antwerp, Belgium (permit number 2016–17) and all efforts were made to ensure animal well-being.

2.2. Animals

TgF344-AD and WT littermates breeding pairs were purchased from the group of Prof. Terrence Town at the University of Southern California who developed this strain (Cohen et al., 2013). More specifically, TgF344-AD rats were generated on a Fischer 344 background, bearing the Swedish mutant human amyloid precursor protein (APPswe) and Δ exon 9 mutant human presenilin 1 (PSEN1ΔE9) genes driven by the mouse prion promotor. TgF344-AD and WT were mated and heterozygous TG rats and WT littermates were obtained. WT and TgF344-AD littermates genotypes were determined from ear snips using real time PCR with specific probes designed for each transgene (Transnetyx, Cordova, TN). AD-related pathology in this rat model entails a moderate increase in levels of soluble amyloid β, p-tau and gliosis from 6 months of age and increasing further with age. Also, an impaired entorhinal-hippocampal synaptic transmission is already present at this early age. This is followed by amyloid β plaque formation, neurofibrillary tangles as well as neuronal loss and progressive synaptic and cognitive dysfunction (Bazzigaluppi et al., 2018; Cohen et al., 2013; Joo et al., 2017; Pentkowski et al., 2018; Rorabaugh et al., 2017; Smith and McMahon, 2018; Voorhees et al., 2017).

A total of 23 animals were used for longitudinal MR acquisitions, of which 7 WT and 8 TG animals were afterwards used for *ex vivo* analyses. An additional group of 10 WT and 9 TG rats were used for *ex vivo* analyses at 10 and 16 months of age. All animals were housed in a temperature- and humidity-controlled room on a 12-h light-dark cycle with standard food and water available at libitum.

2.3. Animal handling

A total of 23 female TgF344-AD rats (11 TG, 12 WT) was subjected to MRI procedures in a longitudinal manner at the ages of 6, 10, 12, 16 and 18 months (body weights, see Table S1). Two WT animals were excluded from the study as they developed a brain tumour. All imaging experiments were performed on spontaneously breathing rats under isoflurane (Isoflo®, Abbot Laboratories Ltd.) anaesthesia (5% for induction, 2% for set-up on the animal bed and maintenance), administered in a gaseous mixture of 30% O_2 and 70% N_2. For the rsfMRI acquisition, a bolus of 0.05 mg/kg medetomidine (Domitor, Pfizer, Karlsruhe, Germany) was administered subcutaneously (s.c.) and 5 min

afterwards, isoflurane was reduced and kept at 0.4%. Continuous infusion of medetomidine was started 15 min after bolus injection at a dose of 0.1 mg/kg/h to maintain the sedation level as it has been shown before that this anaesthesia regime is optimal for longitudinal resting state functional connectivity measurements (Grandjean et al., 2014a; Paasonen et al., 2018). After the rsfMRI procedures, isoflurane levels were gradually increased to make sure the animals remained stable for the DTI and 3D acquisition. After the MRI procedures, the effect of medetomidine was counteracted by injecting 0.1 mg/kg atipamezole (Antisedan, Pfizer, Karlsruhe, Germany) and animals were monitored closely until full recovery.

To immobilize the head in a reproducible flat-skull position during the MRI experiments, animals were secured in an MRI compatible rat stereotactic device. The head was held by a nose cone used for anaesthetic gas delivery, including tooth bar and blunt earplugs. An actively decoupled surface array (2 × 2) receiver coil was positioned on top of the head. Respiration rate, monitored with a small animal pressure pad (MR-compatible Small Animal Monitoring and Gating System, SA instruments, Inc.), was maintained within normal physiological ranges. Rectal temperature was maintained at (37.0 ± 0.5) °C using a feedback coupled warm air system (MR-compatible Small Animal Heating System, SA Instruments, Inc.). Blood oxygenation was monitored using a fibre optic pulse oximetry sensor (SA instruments, Inc.) positioned on the foot of the rats.

2.4. Image acquisition

Experiments were performed on a Bruker Pharmascan 7 T imaging system (Bruker, Ettlingen, Germany). To ensure uniform slice positioning, 2D Turbo RARE T_2-weighted images were acquired for each individual animal along three orthogonal directions to assess the subject's position (RARE; TR 2500 ms; TE 33 ms; 10 slices of 1 mm; FOV (30 × 30) mm^2; pixel dimensions (0.12 × 0.12) mm^2). Field maps were acquired for each animal, followed by local shimming, which corrects for the measured inhomogeneity in a rectangular volume of interest (VOI) within the brain, covering the FOV of the DTI and rsfMRI. The timeline of the total experimental protocol with the different imaging modalities is illustrated in Fig. S1 A.

RsfMRI acquisition was performed using a 2D T_2*-weighted single shot gradient echo (GE) echo planar imaging (EPI) sequence (2D GE-EPI; TR 2000 ms; TE 29 ms; 20 coronal slices of 0.7 mm, slice gap 0.1 mm; 300 repetitions, frequency-encoding left-right). The field-of-view (FOV) was (30 × 30) mm^2 and the matrix size [128 × 128], resulting in voxel dimensions of (0.234 × 0.234 × 0.8) mm^3. RsfMRI scans were acquired 40 min after the initial bolus administration and the total scan time was 10 min. The slice package covered a large part of the brain (Fig. S1 B) ranging from approximately Bregma 5.16 mm to Bregma −8.88 mm.

DTI scans were acquired using a two-shot spin echo (SE) EPI sequence (2D DW-SE-EPI; TR 7500 ms; TE 26 ms; 20 coronal slices of 0.7 mm, slice gap 0.1 mm, b-value 800 s/mm^2, diffusion gradient pulse duration δ 4 ms, diffusion gradient separation Δ 12 ms, frequency-encoding left-right), with diffusion sensitizing gradients applied along 60 optimally spread different directions. Fifteen b_0 images were acquired (b = 0 s/mm^2; 5 b_0 images per 20 diffusion weighted images) and the total acquisition time was approximately 20 min. The FOV was (30 × 30) mm^2 with a [128 × 128] acquisition matrix, resulting in a resolution of (0.234 × 0.234 × 0.8) mm^3. The slice package was similar to the rsfMRI acquisition (Fig. S1B).

3D images were acquired using a 3D RARE sequence (TR 3185 ms; TE 44 ms; RARE factor 8; frequency-encoding head-foot). The matrix size was [256 × 64 × 50] and FOV (29 × 16 × 10.2) mm^3 resulting in a voxel resolution of (0.11 × 0.25 × 0.20) mm^3 with a total scan duration of 43 min.

2.5. rsfMRI data analysis

Pre-processing of the rsfMRI data, including realignment, normalization and smoothing, was performed using SPM12 software (Statistical Parametric Mapping, http://www.fil.ion.ucl.ac.uk, (Hamaide et al., 2017; Jonckers et al., 2011)). First, all images within each session were realigned to the first image. This was done using a least-squares approach and a 6-parameter rigid body spatial transformation. Second, rsfMRI images were co-registered to the 3D RARE data of the same imaging session using a rigid body model with mutual information as the similarity metric. In parallel, the 3D RARE data was spatially normalized to match a study-specific 3D-template, obtained in ANTs (Advanced Normalization Tools), using a global 12-parameter affine transformation followed by a nonlinear deformation protocol. Next, the transformation matrix of the spatial normalization was applied to the realigned and co-registered rsfMRI images while preserving the original voxel sizes. Afterwards, in-plane smoothing was done using a Gaussian kernel with full width at half maximum of twice the voxel size (FWHM = 0.468 mm × 0.468 mm). Finally, the Resting State fMRI Data Analysis toolbox (REST 1.8, http://resting-fmri.sourceforge.net) was used to filter the rsfMRI data. The filter was set between 0.01 and 0.1 Hz to rule out noise and low frequency drift and retain the low frequency fluctuations of the time course of the BOLD-signal that are of interest when performing FC studies.

Independent Component Analysis (ICA) was performed on the rsfMRI data as described earlier (Jonckers et al., 2011) to determine which resting-state networks could be observed within the population examined using a design entailing all data sets (2 groups, 5 time points). Group ICA was performed using the GIFT-toolbox (Group ICA of fMRI toolbox, version 3.0a: http://icatb.sourceforge.net/). The number of components was set to 20. Anatomically relevant components were identified (Table 1, Fig. S2) based on a 3D anatomical template and with reference to the rat brain anatomical atlas (Paxinos and Watson, 2007). Components were named depending on the region where the peak intensity was observed.

The spatial maps derived from this data-driven analysis were then used to evaluate inter-regional and intra-regional FC. First,

Table 1
Overview of the main regions obtained from the anatomically relevant ICA components.

Abbreviation	Region	Abbreviation	Region
M1	Primary motor cortex	$V2_{MM-ML}$/V1	Secondary visual cortex, mediomedial and mediolateral area / Primary visual cortex
$S1_{HLFL}$	Primary somatosensory cortex, forelimb and hindlimb region	Au_{D-V}/Au1	Secondary auditory cortex, dorsal and ventral area / Primary auditory cortex
$S1_{ULp}$/S2	Primary somatosensory cortex, upper lip region / Secondary somatosensory cortex	Cg2	Cingulate cortex, area 2
$S1_{HLFL}$/M1	Primary somatosensory cortex, forelimb and hindlimb region / Primary motor cortex	Cg1/RS	Cingulate cortex, area 1 / Retrosplenial cortex
$S1_{BF}$	Primary somatosensory region, barrel field	RSG	Retrosplenial granular cortex
$S1_{Tr}$ L	Primary somatosensory cortex, trunk region, left	HC	Hippocampus
$S1_{Tr}$ R	Primary somatosensory cortex, trunk region, right	CPu	Caudate putamen

anatomically relevant ICA components were transformed into anatomical ROIs for further analysis. To assess the connectivity between regions, *i.e.* inter-regional FC, the average BOLD time course was extracted from each ROI for every individual scan. Next, correlation coefficients were calculated between the time courses of each pair of regions. These correlation coefficients were z-transformed, resulting in a correlation matrix. Mean z-transformed FC (zFC) matrices were calculated for each group.

Using the group-level ICA component spatial map as reference, seed regions of four voxels each were manually indicated in MriCron software at the peak intensity (T_{max}) of the relevant component and used to extract the respective temporal signal of each subject (14 seeds, see Table 1). This signal was then used to obtain the individual FC maps as described previously (Shah et al., 2016a). Briefly, the extracted temporal signal was compared to all other voxels within the brain, resulting in FC maps containing voxels significantly correlated with the given temporal signal. Intra-regional FC was calculated as the average correlation strength of all voxels within the corresponding group-level ICA component mask with the given seed.

2.6. DTI data analysis

Pre-processing of the diffusion data was performed using SPM12 software as described previously (Hamaide et al., 2017). Briefly, images were realigned to correct for subject motion using the Diffusion II toolbox in SPM12. A rigid registration was performed between the b_0 images, which was followed by an extended registration taking all DW images into account. Next, the realigned DW images were co-registered to the 3D RARE data set of the same imaging session and normalized to match the study-specific 3D template using the same procedure as the rsfMRI data. Then, the diffusion tensor was estimated and DTI parameter maps were computed, *i.e.* fractional anisotropy (FA), mean diffusivity (MD), axial diffusivity and radial diffusivity. Finally, all DTI parameter maps were smoothed in-plane using a Gaussian kernel with FWHM of twice the voxel size (FWHM = 0.468 mm × 0.468 mm). Next to a voxel-based analysis (VBA), a ROI-based analysis was performed by overlaying ROIs on the individual normalized maps and extracting the average DTI parameter value. Care was taken to ensure proper registration of the DTI parameter maps as well as correct positioning of each ROI. This additional ROI-based analysis was guided by the outcome of the rsfMRI data and included the cingulate, retrosplenial and hippocampal brain regions. Lastly, the entorhinal cortex was included to verify the obtained VBA results. ROIs were manually defined in AMIRA 5.4.0 software with the original corresponding ICA component, rat brain atlas (Paxinos and Watson, 2007) and an in-house rat brain ROI atlas as reference.

2.7. 3D RARE data analysis

3D RARE data were analyzed using a ROI-based analysis and a tensor-based morphometry (TBM) analysis to assess local volume changes (Ashburner, 2015). Pre-processing of the 3D RARE data was performed in SPM12 software. A serial longitudinal registration (SLR in SPM12) was performed between the five individual 3D scans of an individual subject. Briefly, this step entailed the alignment of every scan to the intra-subject template using an intensity non-uniformity (bias field) correction followed by a rigid-body transformation and nonlinear registration steps (Ashburner and Ridgway, 2012). During the SLR, the intra-subject template, or mid-point average corresponding to the 12 month time point, was created and Jacobian determinants were obtained. These determinants describe the relative local shape difference, *i.e.* expansion (> 1) or contraction (< 1) of a voxel due to the non-rigid deformation compared to the template. Next, these Jacobian determinants were normalized to the study-specific 3D template using a similar procedure as described above in order to perform voxel-based analyses. During this step, Jacobian determinants were modulated to preserve relative volume differences existing between different subjects. A final step included in-plane smoothing using a Gaussian kernel with FWHM of twice the voxel size (0.22 × 0.50) mm^2.

Additionally, the study-specific 3D template was used by the FMRIB Automated Segmentation Tool (FAST; (Zhang et al., 2001)) embedded in FSL, to extract tissue probability maps reflecting mainly grey matter, white matter and cerebrospinal fluid. The three probability maps created in this step were used as tissue class *priors* for segmenting the individual midpoint averages in SPM12. In parallel, a whole brain mask for the 3D template as well as a hippocampal ROI were manually delineated in Amira 5.4.0 software. After back projection of the 3D template whole brain mask as well as the hippocampal ROI and midpoint average tissue segments to the individual scans in native space, volumes were extracted for whole brain, grey matter (GM), white matter (WM), cerebrospinal fluid (CSF) and hippocampus. Relative volumes were calculated by dividing the tissue volumes by the absolute whole brain volume.

2.8. Ex vivo pathology

At the ages of 10 ($N_{WT} = 6$; $N_{TG} = 5$), 16 ($N_{WT} = 4$; $N_{TG} = 4$) and 18–20 months ($N_{WT} = 7$; $N_{TG} = 8$), brain tissue samples were acquired for *ex vivo* pathology analyses. Following transcardial perfusion with 0.9% NaCl, brains were dissected and fixed by immersion in 0.1 M phosphate buffered 4% paraformaldehyde pH 7.4 for 4 h. After washing with PBS, brains were transferred in 0.1 M phosphate buffered 30% sucrose solution pH 7.4 at 4 °C for at least 48 h. Brains were then cut in 40 µm sagittal sections using a sliding microtome (Leica) on dry ice and sections were serially collected into 10 tubes containing cryoprotectant solution (25% *v*/v glycerol, 0.05 M sodium phosphate buffer pH 7.4, 25% v/v ethylene glycol), each tube containing 1/10 of a hemisphere with 400 µm inter-section separation. Series were thereafter stored at −20 °C until processing.

Following antigen-retrieval with citrate buffer pH 6.0 (Sigma-Aldrich, C9999) for 1 min at 100 °C, fluorescent immunohistological labelling was performed as previously described (Adamczak et al., 2017). Primary antibodies: mouse anti-Amyloid beta (Covance, SIG-39300) 1:500; rabbit anti-Iba1 (Abcam, ab178846) 1:1000; guinea-pig anti-GFAP (Progen, GP52) 1:500; guinea-pig anti-NeuN (Millipore, MAB377) 1:500. Secondary antibodies: donkey anti-mouse Alexa 488 nm (Invitrogen, A21202) 1:1000, donkey anti-rabbit Alexa 568 nm (Invitrogen, A10042) 1:1000, donkey anti-guinea-pig Alexa 647 nm (Jackson, 706-605-178) 1:1000. Nuclei were counterstained with DAPI (Sigma-Aldrich, D9564, 0.5 µg/mL). For quantification, fluorescence images were acquired using an Olympus VS120 Slide Scanner and the rat brain atlas from Paxinos and Watson (Paxinos and Watson, 2007) was used as reference to localize the regions of interest (one micrograph per region of interest and rat). Micrographs were further processed with ImageJ Software 1.46r (National Institutes of Health) and FIJI based on ImageJ 1.50a (Schindelin et al., 2012). Microglia ($Iba1^+$ cells) were manually counted. The percentages of area covered by beta-amyloid, GFAP or NeuN were determined in the regions of interest following binarization with fixed detection threshold slightly above background intensity for each marker and age-group. High resolution micrographs for illustration purposes (Fig. S9) were acquired with a Zeiss LSM710 confocal microscope.

2.9. Statistical analyses

Voxel-based statistical analyses of FC maps, DTI parameter maps and Jacobian determinants of the 3D anatomical scans were performed in SPM12 software, where a repeated measures two-way ANOVA design was used to test for the interaction between age and genotype as well as for the main effect of age or genotype. For this, a 2 × 2 factorial design was constructed with genotype (TG, WT) as between-subject factor and age (6, 10, 12, 16 and 18 months) as within-subject factor. To account

for errors induced by multiple comparisons, a family wise error (FWE) correction was applied with $p_{FWE} < 0.05$ and a minimum cluster size of 10 voxels ($k > 10$). Besides this very stringent correction, all statistical maps were assessed with a more liberal false discovery rate (FDR) correction ($p < 0.05$) and a minimum cluster size of 10 voxels. All statistical voxel-based maps are shown overlaid on an anatomical 3D study-specific template (displayed FDR $p < .05$; minimum 10 voxels). Results are reported by the highest voxel F_{max} or T_{max} value and the associated voxel p_{FWE} and p_{FDR} value (peak-level p). In case a significant interaction [age x genotype] effect or main effect of age or genotype was found according to the voxel-based analysis, data within these clusters were extracted from each individual scan and plotted in a graph for further examination.

All ROI-based analyses (rsfMRI, DTI and 3D) as well as the differences between body weights of the animals were assessed using a repeated measures two-way ANOVA in Graphpad Prism 6.0 or Matlab to test for the interaction between age and genotype as well as for the main effect of age or genotype. *Post hoc* tests were performed using Sidak's multiple comparisons test with $p < 0.05$. In case multiple analyses were performed in parallel, a false discovery rate (FDR) correction ($p < 0.05$) was applied to account for the multiple testing.

Ex vivo data were analyzed in Graphpad Prism 6.0 where a two-way ANOVA design was used to test for the interaction between age and genotype as well as for the main effect of age or genotype. *Post hoc* Sidak's multiple comparisons tests were applied with $p < 0.05$. For the analysis of the amyloid plaque load in the TgF344-AD rats, a one-way ANOVA with Tukey's *post hoc* tests ($p < 0.05$) was used to assess the age-dependent effect.

All results are shown as mean ± SEM (standard error of mean). When no significant [age x genotype] interaction was found, only main effects for age and genotype are reported.

3. Results

3.1. Reduced functional connectivity between brain regions

A group ICA analysis was performed using a pre-set of 20 components, of which 14 were classified to be anatomically relevant (Fig. S2). The selected components could be identified as cortical networks, *i.e.* sensorimotor cortical components or cingulate and retrosplenial components, and subcortical networks. Other, irrelevant, components included noise and blood vessel artifacts. Based on the regions obtained from this ICA outcome, an inter-regional FC analysis was performed to assess the functional connectivity between the different regions ~~networks~~ at every time point (Fig. 1). As no significant [age × genotype] interaction survived the FDR correction, only main effects are reported. A significant genotype effect indicating widespread decreased FC in TG rats compared to WT rats was found for almost all connections. CPu, $S1_{HL\text{-}FL}$ and $S1_{ULp}$-S2 regions did not show any significantly altered connections with any other region (Fig. 1 F). An examination of the overall (whole brain) average inter-regional FC at every time point confirmed that TG rats had consistently reduced FC values compared to WT ($F_{1,18} = 20.62$, $p = 0.0003$), with the largest difference occurring at 10 months of age (−17%).

To further elucidate how this decreased FC in TG animals evolved along disease progression, connections displaying a main effect of genotype were examined in more detail. This revealed only decreased FC in TG rats as compared to WT, without signs of significantly increased FC in the TG group (Fig. 1 G, Fig. S3). As early as 6 months of age, slightly decreased FC values were present in TG rats for several connections with the hippocampus, cingulate and retrosplenial cortices, and sensorimotor regions. This effect progressed towards an overall severely reduced FC at the age of 10 months, with most connections showing a strong significant decrease in TG animals compared to WT. This reduced FC in TG rats persisted at later time points, although somewhat less pronounced throughout the brain. Important to note is that connections between typical brain regions involved in AD, such as the cingulate, retrosplenial and hippocampal regions, were decreased in TG animals starting at 10 months. Especially connections between hippocampal, cingulate and retrosplenial regions showed an age-dependent increasing difference between WT and TG animals. Beside the genotype differences, slight age-dependent alterations were present in both groups (Fig. 1 F) for connections with the CPu and M1 regions, reflecting an age-dependent FC reduction. In contrast, FC between $V2_{MM\text{-}ML}$/V1–HC and $Au_{D\text{-}V}$/Au1-HC displayed a significant increase when comparing young (6–10 months) and older (16–18 months) ages.

Because the largest FC differences were observed at 10 months of age, which then slightly diminished towards 16 months of age, an additional examination of age-dependent effects in these time intervals was performed. More specifically, the average monthly change of FC was computed for the time intervals between 6 and 10 months of age as well as between 10 and 16 months of age for both TG and WT animals. It can be appreciated from Fig. S4 that a differential effect was present for each genotype. As such, WT animals displayed an overall strengthening of FC between 6 and 10 months, whereas TG FC values remained fairly low (Fig. S4 A). In contrast, an age-dependent strengthening of FC in TG animals only occurred between 10 and 16 months of age (Fig. S4 B). In this time interval, WT animals showed a further strengthening of several connections with HC, $V2_{MM\text{-}ML}$/V1 and $Au_{D\text{-}V}$/Au1 regions. Although no significant interaction effects of [genotype x time interval] survived the FDR correction, it can still be appreciated that this seemingly opposite effect was most pronounced in the following connections: $S1_{BF}$-Cg1/RS ($F_{1,18} = 11.5$; $p = 0.07$); $S1_{Tr}$L-RSG ($F_{1,18} = 11.6$; $p = 0.07$); $V2_{MM\text{-}ML}$/V1-RSG ($F_{1,18} = 11.4$; $p = 0.07$); $S1_{Tr}$L-Cg1/RS ($F_{1,18} = 10.2$; $p = 0.08$); $Au_{D\text{-}V}$/Au1-RSG ($F_{1,18} = 9.15$; $p = 0.09$).

3.2. Reduced local functional connectivity

To assess the functional connectivity within a certain region, the individual temporal BOLD signal was extracted from the relevant seed and used to calculate intra-regional FC (Fig. S5). Consistent with the inter-regional analysis, lower FC values were present in the TG group compared to WT in auditory regions ($F_{1,18} = 13.13$; $p = 0.0067$), cingulate/retrosplenial cortex ($F_{1,18} = 13.69$; $p = 0.0067$), frontal cingulate cortex ($F_{1,18} = 21.02$; $p = 0.0021$), hippocampus ($F_{1,18} = 6.64$; $p = 0.038$), retrosplenial cortex ($F_{1,18} = 10.35$; $p = 0.0134$), the right $S1_{Tr}$ region ($F_{1,18} = 7.38$; $p = 0.0329$) and the visual cortices ($F_{1,18} = 19.65$; $p = 0.0021$). Furthermore, an age-dependent increase of FC was present in both groups for the motor ($F_{4,72} = 4.00$; $p = 0.0252$), retrosplenial regions ($F_{4,72} = 3.80$; $p = 0.0259$), visual ($F_{4,72} = 4.33$; $p = .0238$) and auditory cortices ($F_{4,72} = 6.24$; $p = 0.0028$). This age-dependent change was already evident in WT animals between 6 and 12–18 months, whereas TG animals only displayed an age-dependent increase after 10 months of age.

As the strongest local (*i.e.* intra-regional) reduction of FC was found for the frontal cingulate cortex (Cg2), an illustration of localized genotype differences of the intra-regional FC, by means of a seed-based analysis, is shown in Fig. 2 for this region. A significantly reduced FC was present in TG animals compared to WT animals (Fig. 2 A; $p_{FWE} < 0.0001$; $p_{FDR} < 0.001$; 976 voxels; $F_{max} = 46.01$). Also an age-dependent alteration of FC was present in a cluster of 352 voxels ($p_{FWE} < 0.0001$; $p_{FDR} < 0.001$; $F_{max} = 12.85$; Fig. 2 B). When plotting the corresponding FC values (Fig. 2C), the strongest difference between TG and WT rats was present at 10 months of age. TG animals presented a minor increase of FC between 10 and 16 months of age, resulting in slightly smaller genotype differences at later ages. Note that these results differ slightly as compared with Fig. S5, when taking into account the entire region rather than only the localized significant genotype effect as presented in Fig. 2.

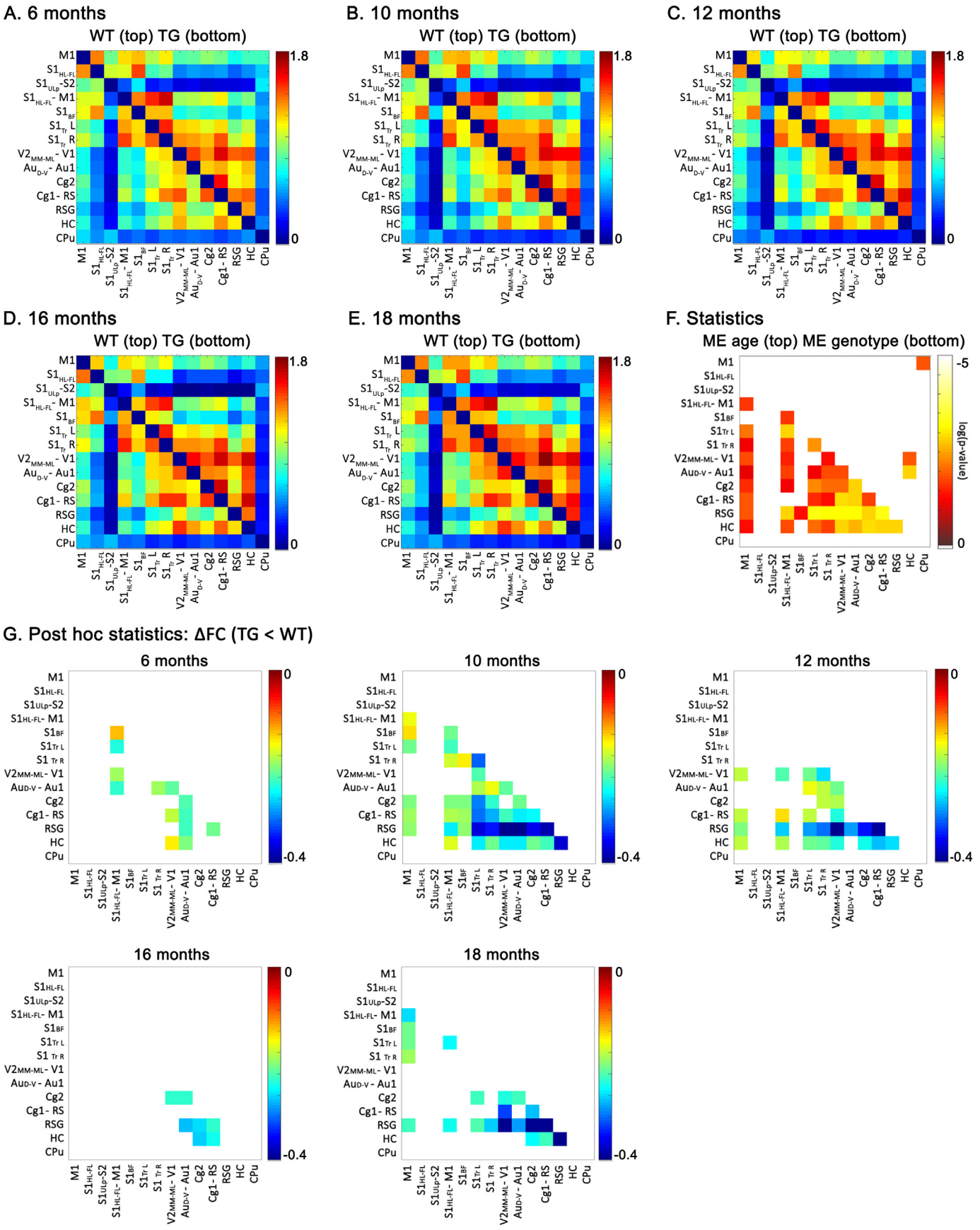

(caption on next page)

Fig. 1. Inter-regional FC analysis. A-E. Every matrix shows the average z-transformed functional connectivity (zFC) for both WT (top half) and TG (bottom half) animals. Each square indicates the zFC between a pair of ROIs. The colour scale represents the strength of the connectivity with green/blue indicating a low zFC and yellow/red indicating higher zFC values. Abbreviations of regions: see Table 1. F. Main outcome of the statistical analysis. No significant [age x genotype] interaction was found below the FDR correction of $p < 0.05$, so only significant main effects are reported. The bottom half of the matrix shows the main effect of genotype, whereas the main effect of age is shown in the top half of the matrix. The colour scale represents the log(*p*-value), with yellow indicating a lower p-value. G. Results of the *post hoc* tests showing significantly reduced FC in TG animals. The colour scale indicates the difference (ΔFC) between WT and TG (corresponding to significant *p*-values, $p < 0.05$) with blue indicating a stronger decrease in TG animals compared to WT. (For interpretation of the references to colour in this figure legend, the reader is referred to the web version of this article.)

3.3. Progressive microstructural alterations

To evaluate whether microstructural changes could be observed in TG rats, a voxel-based analysis of the DTI parameter maps was performed. As illustrated in Fig. 3 and Table S2, several clusters were found to be significantly altered in TG animals compared to WT, for both FA and MD.

More specifically, decreased MD values were present in the ventricular regions of the TG animals, whereas MD was significantly elevated in the primary motor and somatosensory cortex (Fig. 3 A; Table S2). When lowering the threshold from a stringent FWE-corrected to FDR-corrected $p < 0.05$, an additional cluster in the subgeniculate nucleus appeared, with higher MD values in TG animals compared to the WT group. An age-dependent decline of MD for both groups was found in clusters in the striatum, internal capsule, corpus callosum, and part of the external capsule (Fig. S6 A). Between 6 and 10 months of age, the strongest reduction was observed for both groups, which was followed by a minor reduction between 12 and 18 months of age mainly in WT animals (data not shown).

An investigation of FA (Fig. 3 B; Table S2) revealed that TG animals had strongly decreased FA values in a large bilateral cluster comprised of the ventral part of the external capsule stretching into the entorhinal cortex. TG rats showed a progressive decrease of FA within this region starting at 10 months of age leading up to a 10% decrease at 18 M of age compared to WT. Importantly, a ROI-based analysis of the full entorhinal cortex confirmed this result showing a similar age-dependent progressive decrease of FA (data not shown), which is in agreement with previous studies showing early AD pathology in this brain region (Rorabaugh et al., 2017). When lowering the threshold from a stringent FWE-corrected to a more exploratory FDR-corrected $p < .05$, additional bilateral cortical clusters were found, located in the motor (M1) and somatosensory ($S1_{BF}$, $S1_{HL\text{-}FL}$) cortex. Again, lower FA values were present in TG animals as compared to WT animals. In contrast, increased FA values were present in a cluster comprising the corpus callosum and dorsal part of the external capsule. Also, a small section of the lateral somatosensory cortex (S2, $S1_{ULp}$) showed higher FA in TG animals compared to WT.

Age-dependent alterations of FA were present in both groups in bilateral cortical clusters, as well as in the cingulum (Fig. S6 B). *Post hoc* tests within these main effects, revealed that an age-dependent decline of FA in these regions started between 6 and 10 months for the cortical regions and between 12 and 16 months for the cingulum (data not shown). Importantly, age-dependent alterations were again most pronounced in the WT animals.

Axial and radial diffusivity measures also differed between WT and TG animals (data not shown). As such, both axial and radial diffusivity values were significantly lower in TG rats in the ventricular area and elevated in cortical areas, similar to changes of MD. Additionally, axial diffusivity was significantly lower in the ventral part of the external capsule and increased in the corpus callosum, similar to FA. In line with age-dependent changes of FA and MD, respectively, age-dependent alterations of axial diffusivity were present in the cingulum and anterior cingulate cortex, corpus callosum and the external capsule, whereas radial diffusivity showed an age-dependent attenuation in the caudate putamen.

An additional ROI-based analysis (Fig. 4) was performed to further examine regions characteristically involved in AD, *i.e.* the cingulate regions and hippocampus (Weston et al., 2015). Importantly, these regions were also identified to be affected in the rsfMRI data. The cingulate and hippocampal ROIs were similar to the rsfMRI analysis to identify potential co-existing functional and structural alterations as FC in these regions was found to be severely affected. As described before, TG animals had significantly lower FC both within and between the Cg2 and Cg1RS regions. The corresponding DTI parameters showed a

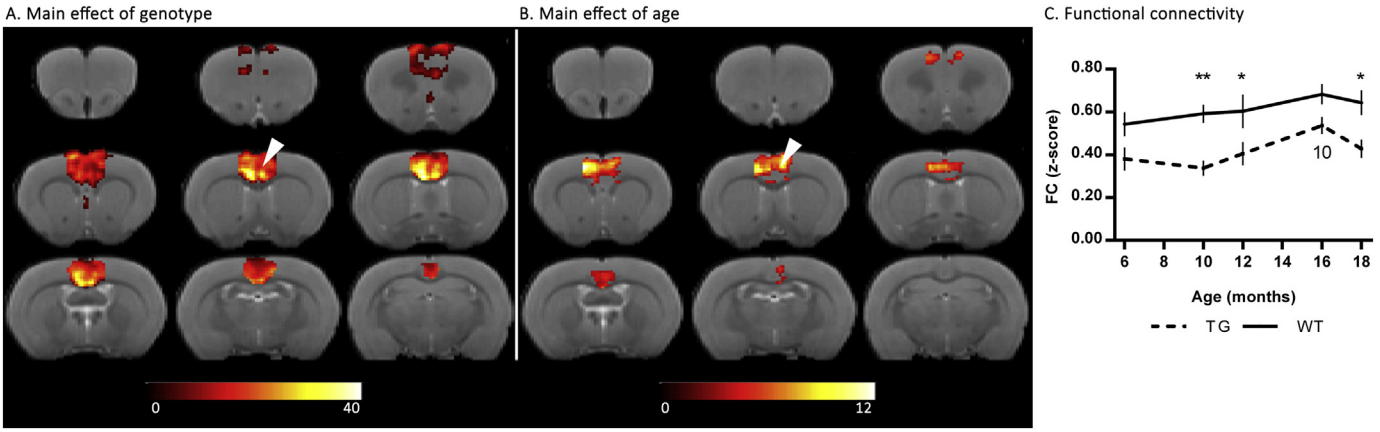

Fig. 2. Intra-regional FC analysis for the frontal cingulate cortex by means of a seed based analysis. A-B. Outcome of a voxel-based analysis of the Cg2 FC maps, with arrowheads indicating the location of the seed (four voxels). A main effect of genotype (A, TG < WT) is present throughout the region, whereas only a small cluster shows an age-dependent alteration (B). Note that this age-dependent change was mainly driven by an increase of FC between 10 and 16 months in TG animals (C). The colour scale represents f-values with yellow indicating a larger difference between the conditions investigated. All results are shown on an anatomical 3D-template, FDR-corrected $p < 0.05$ and a minimum cluster size of 10 voxels. C. Evolution of FC within the restrictions of the cluster showing a main effect of genotype (A). Stars indicate significant differences between TG and WT, with *$p < 0.05$; ** $p < 0.01$. Age-dependent alterations are indicated with numbers representing significant differences compared to the indicated time point (*e.g.* '6' indicates a significant difference between that respective time point and the 6 month time point of the same group). (For interpretation of the references to colour in this figure legend, the reader is referred to the web version of this article.)

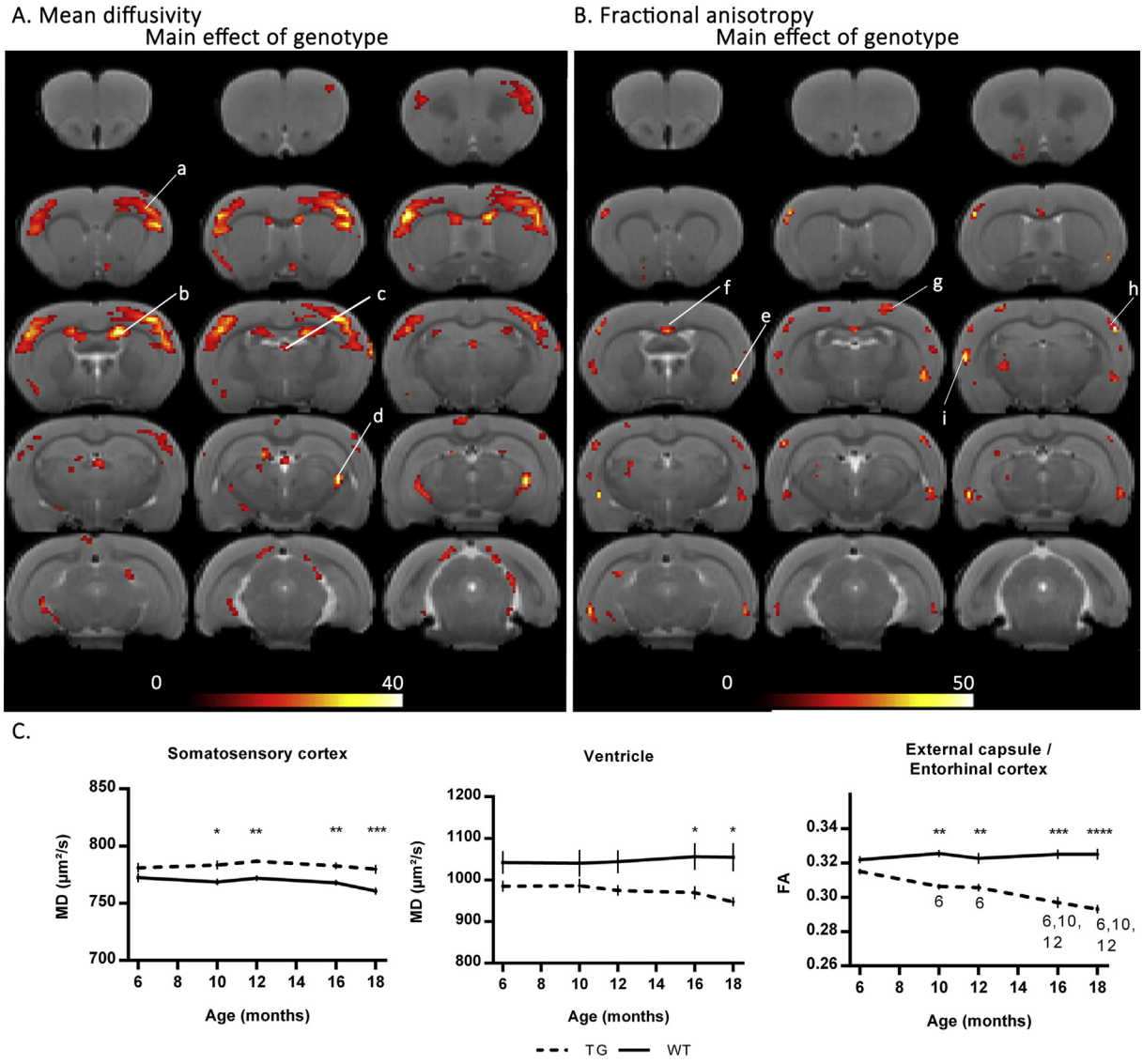

Fig. 3. Voxel-based statistical analysis of DTI parameters, MD and FA. Significant main effects of genotype are shown for both MD (A) and FA (B). Results are displayed on an anatomical template, with a visualization threshold of FDR $p < 0.05$ and a minimum cluster size of 10 voxels. The colour scale indicates f-values with yellow indicating a larger difference between the conditions investigated. a. Primary motor and somatosensory cortex (M1, M2, $S1_{HL\text{-}FL}$; $S1_{ULp}$); b. Lateral ventricle; c. Third ventricle; d. Subgeniculate nucleus; e. External capsule/entorhinal cortex; f. corpus callosum; g. Sensorimotor cortex (M1, $S1_{HL\text{-}FL}$); h. Somatosensory cortex ($S1_{BF}$, $S1_{HL\text{-}FL}$); i. Lateral somatosensory cortex (S2, $S1_{ULp}$). C. The strongest effects according to the VBA are plotted in graphs. Stars indicate significant differences between TG and WT, with *$p < 0.05$; **$p < 0.01$; ***$p < 0.001$; ****$p < 0.0001$. Age-dependent alterations are indicated with numbers representing significant differences compared to the indicated time point (*e.g.* '6' indicates a significant difference between that respective time point and the 6 month time point of the same group). (For interpretation of the references to colour in this figure legend, the reader is referred to the web version of this article.)

significant interaction effect of [age x genotype] for FA (Cg2: $F_{4,64} = 3.043$; $p = 0.0233$; Cg1RS: $F_{4,64} = 3.873$; $p = 0.007$). *Post hoc* tests indicated that for both regions TG and WT animals differed most at more advanced ages. In the Cg2 region (Fig. 4 A), this effect was due to an age-dependent decline of FA in the TG group (−3% between 6 M and 16 M, $p = 0.0069$; −4% between 6 M and 18 M; $p = 0.0005$), whereas WT values remained stable over time. In contrast, although WT animals presented an age-dependent increase of FA in the Cg1RS region (+4% between 6 M and 16 M; $p = 0.0156$), no change was present for the TG group leading to a difference between both groups of 5% at this advanced stage (Fig. 4 B). This coincided with significantly increased MD ($F_{1,18} = 8.519$; $p = 0.0092$) and RD values ($F_{1,17} = 12.02$; $p = 0.003$) in the Cg1RS region of TG animals. In the hippocampus, significantly lower FC co-existed with decreased FA values ($F_{1,16} = 9.949$; $p = 0.0061$) in TG animals (Fig. 4 C). It can be appreciated from the graph that this decreased FA in TG animals was aggravated at more advanced age due to a minor (non-significant) decrease of −2.5% in TG animals at 18 months compared to 6 months. Important to note is that whereas these regions did not appear in the VBA (Fig. 3), clusters within these regions were still observed when lowering the threshold further to an uncorrected p-value $p < .05$ (data not shown) corroborating this ROI-based analysis.

3.4. Macroscopic alterations

First, a ROI-based analysis of the whole-brain volume was performed to identify global differences between both groups (Table S3). This analysis revealed a strong trend for enlarged whole brain volumes in TG animals ($F_{1,18} = 3.571$; $p = 0.075$; +2%) throughout the entire experiment. Additionally, an age-dependent increase of whole brain volumes was present in both groups ($F_{4,72} = 18.55$; $p < 0.0001$) as can be appreciated in Table S3. An examination of the relative volumes of

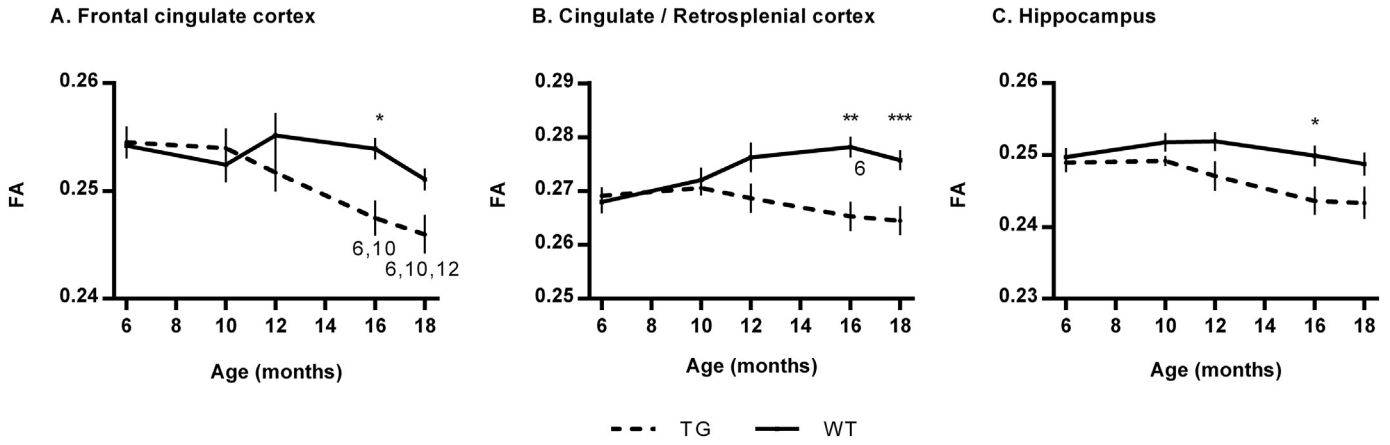

Fig. 4. ROI-based analysis of FA in regions characteristically involved in AD. Stars indicate significant differences between TG and WT, with *p < 0.05; **p < 0.01; ***p < 0.001. Age-dependent alterations are indicated with numbers representing significant differences compared to the indicated time point (*e.g.* '6' indicates a significant difference between that respective time point and the 6 month time point of the same group).

grey matter, white matter, cerebrospinal fluid and hippocampal region revealed no significant difference (data not shown).

Next, a TBM analysis was performed to identify localized macrostructural differences (Fig. S7). Here, we used modulated Jacobian determinants corrected for the initial whole brain volume difference to account for the pre-existing volume difference between both groups. This TBM analysis indicated a differential genotype effect depending on the region investigated which was consistent throughout all ages investigated, indicating a potential transgenic developmental effect rather than a pathology-induced difference (Fig. S7 A). WT animals showed increased Jacobian values in frontal GM regions ($p_{FWE} = 0.001$; $p_{FDR} = 0.003$; $k = 7863$; $T_{max} = 5.55$) as well as in a cluster comprising the raphe nuclei, mesencephalic reticular formation and part of the cerebral peduncle ($p_{FWE} < 0.001$; $p_{FDR} < 0.001$; $k = 5108$; $T_{max} = 8.90$). This reflects slightly larger regional volumes compared to TG animals. In contrast, TG animals had larger relative volumes in the hypothalamic regions ($p_{FWE} = 0.002$; $p_{FDR} = 0.0.03$; $k = 8145$; $T_{max} = 5.31$), posterior cortical regions, including the retrosplenial cortex ($p_{FWE} = 0.001$; $p_{FDR} = 0.002$; $k = 15{,}132$; $T_{max} = 5.61$) as well as bilateral clusters in the primary sensorimotor cortex ($p_{FWE} = 0.001$; $p_{FDR} = 0.002$; $k = 4211$; $T_{max} = 5.56$). Beside these persistent genotype differences, similar age-dependent changes were detected in both groups (Fig. S7 B) which were slightly more pronounced in the WT group. No age-dependent genotype-specific changes were present indicative of potential cortical atrophy or ventricular enlargement in the TgF344-AD group.

3.5. Ex vivo AD pathology

Microglia density, based on the detection of $Iba1^+$ expression, was calculated for the hippocampus, entorhinal cortex, cingulate cortex, somatosensory cortex and thalamus (Figs. 5, 6). The highest density of microglia was observed in the hippocampus regardless of the genotype. However, as early as 10 months of age, a significantly higher microglia density could be detected in TG rats compared to the WT group, within the hippocampal molecular layer ($F_{1,28} = 20.69$; $p < .0001$; $p_{10M} = 0.022$) and in the hilus ($F_{1,28} = 94.59$; $p < .0001$; $p_{10M} = 0.0384$, Fig. 5 A, Fig. 6 D-F). At 16 and 20 months of age, the density of Iba1-expressing cells in the hilus further increased in TG rats and was highly significantly different as compared to the WT-type group ($p_{16M} < 0.0001$; $p_{20M} < 0.0001$). At this time point, the morphology of the microglia was characteristic of the so-called activated microglia and were often positive for amyloid β as a result of their phagocytic activity. Finally, in the 20 month old TG rats, the density of microglia detected in the entorhinal cortex was also higher as compared to the wild-type group ($F_{1,26} = 14.32$; $p = 0.008$; $p_{20M} = 0.0187$). (See Fig. 7.)

Accumulation of amyloid plaques was observed in the hippocampus, cingulate cortex, somatosensory cortex and thalamus as expected also from the MRI measurements (Fig. 5 B). In contrast, the striatum which showed no functional or microstructural deficits, did not accumulate amyloid plaques, but striatal microglia showed morphological signs of mild activation (Fig. 6J-L). Again, the hilus contained the highest deposition of plaques (Fig. 5 B, Fig. 6 A-F) and these significantly increased until 20 months of age ($F_{2,14} = 5.124$; $p = 0.0396$). In the molecular layer of the hippocampus, a significant increase in amyloid plaques took place between 10 and 16 months ($F_{2,14} = 5.032$; $p = .0396$). Although less abundant, the amyloid plaque deposition also significantly increased over time in the cingulate cortex ($F_{2,33} = 3.460$; $p = 0.05$; Fig. 6 A-C, G-I), somatosensory cortex ($F_{2,16} = 5.407$; $p = .0396$) and in the thalamus ($F_{2,17} = 8.552$; $p = 0.0189$). Additionally, amyloid β positive staining could be observed in blood vessels of TG animals at all ages investigated, whereas this effect was not found in WT animals (Fig. 7 C-D Fig. 6). Moreover abundant amyloid β could be detected in the choroid plexus of the 20 month transgenic animals (Fig. 6C).

No significant changes in GFAP or NeuN expression could be detected between age-matched TG and WT animals (data not shown). Nevertheless, neurotoxicity of amyloid plaques could be observed, as the density of NeuN-expressing neurons in the vicinity of the plaques, for example in the somatosensory cortex, was scarce (Fig. 7 A-B Fig. 6). However, this neuronal loss was very local to the plaques and not large enough to be detectable within larger regions of analysis.

4. Discussion

Preclinical studies are of utmost importance to improve our knowledge of the underlying mechanisms of AD and therefore allowing improved early detection of the disease. However, until now most studies have focused on the examination of transgenic mouse models which usually present only one aspect of the disease thus limiting the translational value of these studies. Here, we present the first longitudinal *in vivo* MRI characterization of the TgF344-AD rat model exhibiting all hallmarks of human AD. Using the highly translational methods of rsfMRI and DTI, we have shown that TgF344-AD rats display severely diminished FC at early stages of the disease and that this is followed by progressive microstructural alterations.

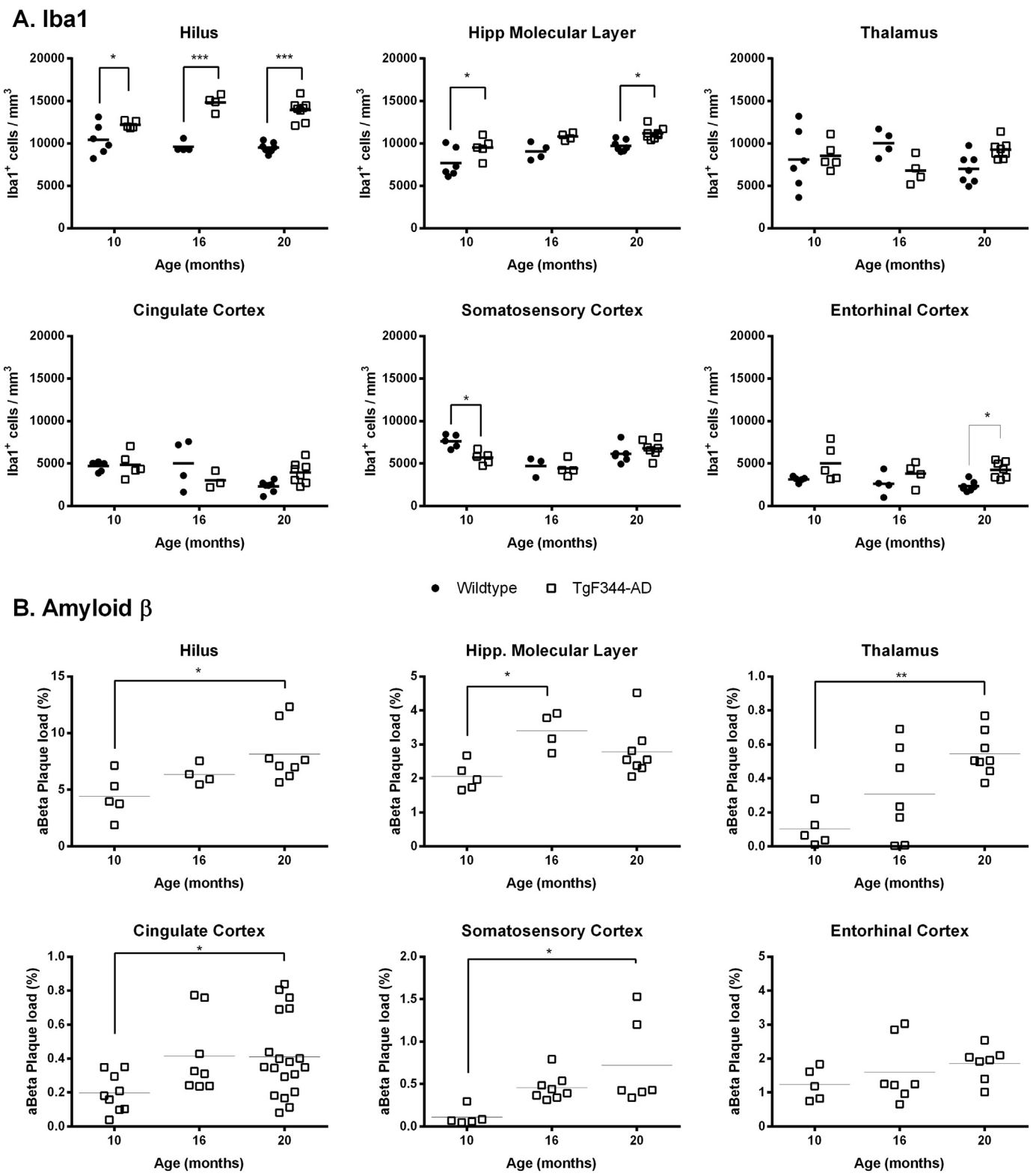

Fig. 5. Quantification of Iba1-expressing microglia (A) and amyloid β load (B) in various regions. * $p < 0.05$; ** $p < 0.01$.

4.1. Reduced functional connectivity precedes microstructural alterations in the TgF344-AD rat

In the present study, we have shown that already at an early stage, *i.e.* six months of age, minor functional deficits could be detected in the absence of microstructural alterations. This included impaired connectivity with the hippocampus, cingulate and sensory regions. At this age, TgF344-AD rats have been previously described to exhibit only low levels of pathological AD characteristics, including elevated concentrations of soluble Aβ, some reactive gliosis and tau hyperphosphorylation, as well as enhanced anxiety-like behaviour (Cohen et al., 2013; Pentkowski et al., 2018; Rorabaugh et al., 2017). Although this early phase of the disease is characterized by only minor pathological hallmarks, the initial rise of Aβ could already lead to synaptic

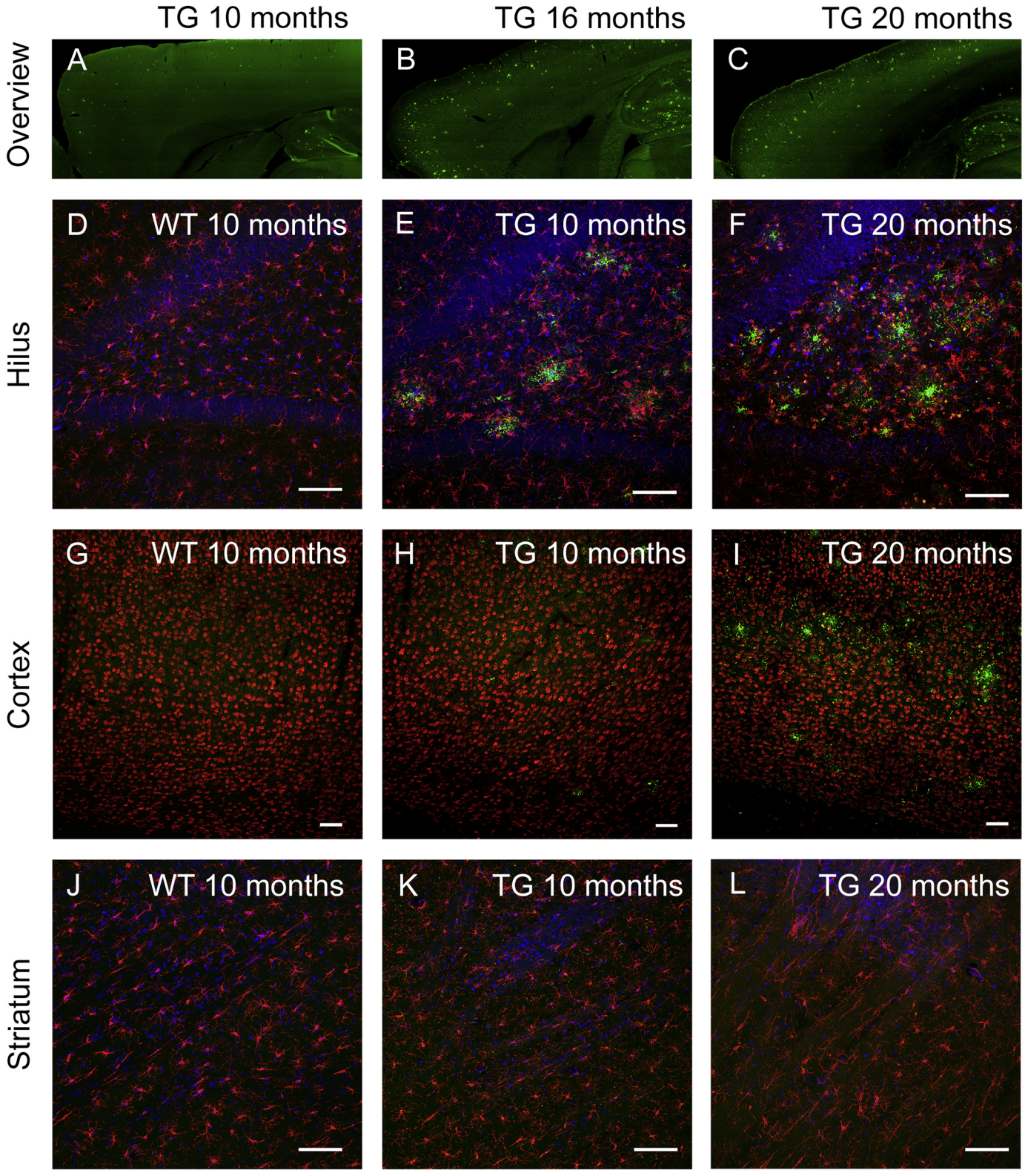

Fig. 6. Illustrative images of *ex vivo* AD pathology. A-C. Overview showing the increase in amyloid β plaque load in the cortical regions of a 10 month, 16 month and 20 month old TG rat. D-F. Age-dependent increase in microglia (Iba1, red) and amyloid β (green) in 10 month and 20 month old TG rats, as compared to a 10 month old WT rat (nuclear counterstain DAPI in blue). G-I. Age-dependent increase of plaque load (amyloid β, green) in the cingulate cortex, without clear evidence of neuronal loss (NeuN, red) in 10 month and 20 month old TG rats, as compared to a 10 month old WT rat. J-L. The striatum did not present significant increase in microglia (Iba1, red) and amyloid β (green) in 10 month and 20 month old TG rats, as compared to a 10 month old WT rat (nuclear counterstain DAPI in blue). (For interpretation of the references to colour in this figure legend, the reader is referred to the web version of this article.)

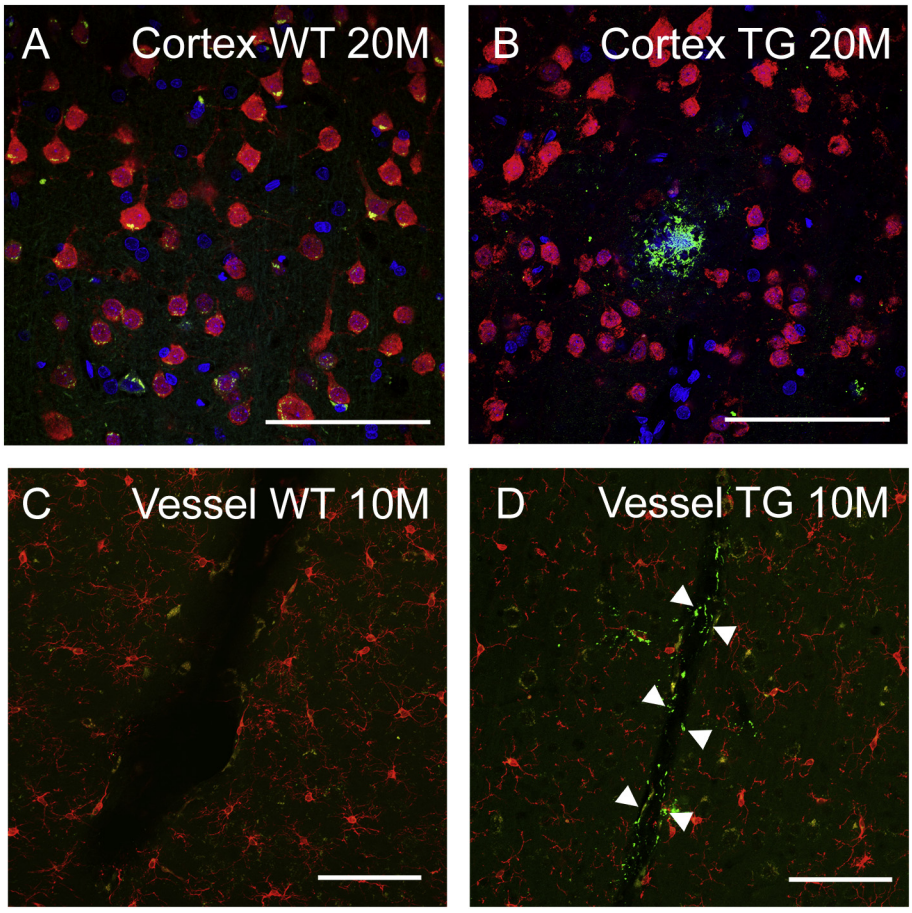

Fig. 7. Illustrative images of neuronal density and cerebral amyloid angiopathy. A-B. Decrease in the neuronal density (NeuN, red) around an amyloid β plaque (green) localized in the somatosensory cortex in 20 month old TG rats as compared to a 20 month old WT rat. C-D. Already at 10 months, the walls of blood vessels in the TG rats, but not WT, showed evidence for cerebral amyloid angiopathy (amyloid β, green). Surrounding microglia are detected with Iba1 (red). Arrowheads indicate the showing amyloid β positive staining on blood vessel walls. Scale bars: 100 µm. (For interpretation of the references to colour in this figure legend, the reader is referred to the web version of this article.)

dysfunction resulting in the observed FC alterations (Mucke and Selkoe, 2012; Selkoe, 2002; Shah et al., 2016a; Smith and McMahon, 2018). The existence of functional hypoconnectivity is in agreement with other rodent and human AD studies, both before and after plaque deposition (Badhwar et al., 2017; Balachandar et al., 2015; Grandjean et al., 2014b). Interestingly, Muñoz-Moreno and colleagues recently used a connectomics approach to evaluate functional and structural network properties in 5 month old male TgF344-AD rats. They reported that early learning and memory deficits in this model are linked with a slightly altered brain functional and structural organisation in regions such as the retrosplenial cortex, entorhinal cortex, amygdala and hippocampus (Munoz-Moreno et al., 2018). Although the animals in that study were cognitively trained before FC assessment, which could alter the FC readout (Nasrallah et al., 2016), these results further support our early FC dysfunction.

In contrast, also hypersynchronous FC has been observed before Aβ deposition in early stages of AD (Quiroz et al., 2015; Shah et al., 2016a). This discrepancy might possibly be explained by differences in timing of FC assessment. As such, hypersynchronous FC could have occurred even before the age of 6 months in the TgF344-AD rat model. It is further important to note that based on the results presented in our study, it is not possible to rule out a potential developmental effect in this rat model of AD due to exposure to the transgenic proteins at early postnatal stages which could affect early brain functional as well as structural development. Future studies could explore brain development in this rat model in more detail to verify this hypothesis.

Consistent with previous reports of neurovascular dysfunction (Bazzigaluppi et al., 2018; Joo et al., 2017), we have identified severely reduced functional connectivity throughout the brain of TG rats at the age of 10 months. Interestingly, this occurred at an age at which still only few pathological hallmarks are present in this rat, as shown by our *ex vivo* analyses as well as others (Bazzigaluppi et al., 2018; Joo et al., 2017; Rorabaugh et al., 2017). Of specific interest are the cingulate cortex and hippocampus, two brain regions classically associated with AD pathology in humans (Selkoe, 2001) and in which strong AD pathology is present in TgF344-AD rats. A severely decreased FC was present both within the regions and with other brain regions, preceding a reduction of FA in these respective brain areas. As described above, initial FC deficits in the absence of clear structural damage are thought to occur due to synaptic alterations (Mucke and Selkoe, 2012). Importantly, BOLD FC measures have a dual vascular and neuronal origin, so vascular dysfunction should also be taken into account (Peca et al., 2013; Princz-Kranz et al., 2010). In line with this, we observed amyloid β positive blood vessels in TG animals across all ages investigated, which agrees with previous data as well. Cohen et al. presented progressive age-dependent cerebral amyloid angiopathy in 16 and 26 month old animals (Cohen et al., 2013). In addition, Joo and colleagues (Joo et al., 2017) showed that even at the age of 9 months, a significant amount of Aβ deposits was present in cortical arterioles. Importantly, they described that loss of vascular contractility at 9 months of age coincided with severe neuronal network dysfunction, as assessed with electrophysiological techniques (Bazzigaluppi et al., 2018; Joo et al., 2017). TgF344-AD rats exhibited decreased neuronal network functioning in the somatosensory cortex, cingulate cortex and hippocampus (Bazzigaluppi et al., 2018; Joo et al., 2017). Moreover, they had a decreased low-gamma resting power in both hippocampus and cingulate region as well as a reduced connectivity between both regions (Bazzigaluppi et al., 2018; Joo et al., 2017). Since there is a strong link between electrophysiological measures and BOLD FC measures (Scholvinck et al., 2010; Weaver et al., 2016), these findings of neuronal network dysfunction are in good agreement with our data showing reduced BOLD-based FC both within and between various

brain regions.

Results presented in this study indicate an overall reduced FC in TG rats compared to WT across all ages investigated (*i.e.* significant main genotype effects), despite progressive AD pathology. Nevertheless, the strongest effect was present at 10 months of age, with connections throughout the entire brain showing a loss of FC compared to age-matched WT. Most connections followed a pattern of no or slightly reduced FC at 6 months, followed by strongly reduced FC at 10 months and slightly dampened, but still significant, hypoconnectivity at more advanced ages. This pattern is likely due to differential age-dependent alterations of FC in both genotypes (Fig. S4). More specifically, WT animals presented an age-dependent strengthening of FC between 6 and 10 months of age, whereas TG animals only showed such strengthening between 10 and 16 months of age.

Of particular interest is the connectivity between hippocampal and cingulate cortical regions, as this connection displayed a different pattern of FC dysfunction. In the present study, no attenuation of this interaction was found at 6 months of age, however, an age-dependent increasing difference was present between WT and TG ranging from a 10% (non-significant) decrease at 6 months to almost 20% at 18 months. Interestingly, disturbances of this interaction have been linked to cognitive deficits in several neuropsychiatric disorders, including AD (Arenaza-Urquijo et al., 2013; Gordon, 2011; Leech and Sharp, 2014; Sampath et al., 2017; Sigurdsson and Duvarci, 2015). This finding could prove to be a valuable *in vivo* marker of pathology in this model, *e.g.* when evaluating new treatment options.

4.2. Progressive microstructural deficits in the TgF344-AD rat

In contrast to the functional data, no or only minor alterations of the microstructural integrity were present in 6 and 10 month old TgF344-AD rats. At 10 months of age, only small unilateral clusters in the frontoparietal somatosensory cortex and the external capsule/entorhinal cortex presented a slightly attenuated MD or FA, respectively. These changes were aggravated in advanced stages of the disease, with large bilateral clusters of increased MD and decreased FA at 18 months. An additional ROI-based analysis further revealed age-dependent alterations in FA of the hippocampus and cingulate cortices. This progressive and age-dependent degenerative pattern seems in line with the *ex vivo* AD pathology in this rat model as shown by us and others (Cohen et al., 2013; Rorabaugh et al., 2017), including progressive amyloid plaque load in various regions and increasing microgliosis in the hippocampus. The histopathology as described here is in good agreement with previous reports of AD pathology in this model (Bazzigaluppi et al., 2018; Cohen et al., 2013; Joo et al., 2017) and could affect the tissue organisation leading to altered diffusion measurements. More specifically, pathology in this rat model was reflected by increased mean diffusivity and decreased anisotropy, which is thought to represent microstructural cellular damage, alterations in tissue organisation, breakdown of diffusion barriers and eventually neuronal loss (Stebbins and Murphy, 2009; Weston et al., 2015). Indeed, a previous *ex vivo* diffusion weighted imaging study in this rat model presented dystrophic neurites in the hippocampus, characterized by enlarged axons and vacuolar pathology, concomitant with age-dependent decreased anisotropy measures (Daianu et al., 2015). Although they used only one animal per age and performed *ex vivo* measurements, these results do support the *in vivo* data as presented here.

Interestingly, according to our VBA DTI data, alterations of MD were most prominent in the sensory cortex in TG animals. Though we could not quantify actual neuronal loss based on the NeuN staining in this region, we did observe a NeuN vacuum around the amyloid plaques. It is possible that NeuN positive dying neurons were phagocytized by microglia, thus complicating the quantification (Voorhees et al., 2017) or that neuronal loss was not yet extensive enough to detect using this method. Nevertheless, neuronal loss has been previously observed in TG rats in cortical and hippocampal regions starting at 16 months of age (Cohen et al., 2013; Voorhees et al., 2017). It has further been suggested that in familial AD an initial decreased MD is present in the presymptomatic phase due to cellular hypertrophy and inflammation (Weston et al., 2015), however, we did not observe this in our study. Future studies could elucidate whether this effect can be detected in this model before the age of 6 months. Alternatively, larger group sizes or different methodologies could prove to be more sensitive to these early changes. Similarly, though it might be hypothesized that MD values decrease at more advanced stages due to cortical thinning, this effect was not observed in the present study. In line with this, the morphometric analysis of the 3D anatomical scans did not reveal significant volume loss typical of AD, *i.e.* cortical or hippocampal atrophy and ventricular enlargement. A possible explanation is that the present study evaluated TgF344-AD rats only up to the age of 18 months, whereas neuronal loss is more extensive at 26 months (Cohen et al., 2013). It is therefore possible that the methods used in our study were not sensitive enough to already detect actual neuronal loss at 18 months or that neuronal loss is not yet that pronounced at this age.

In contrast to the evolution of functional connectivity over time in each group, we observed similar micro-and macrostructural changes between 6 and 10 months in both groups. Only thereafter a slight discrepancy was present between age-related alterations in WT and TG animals, with less pronounced or no changes in the TG group. Again, this corroborates the fact that the early pathological features of AD (mainly soluble amyloid β) affect the functional organisation of the brain prior to structural aspects. It is further likely that the increase of FC between 10 and 16 months is driven by pathological (Shah et al., 2016b) or perhaps compensatory mechanisms (Bobkova and Vorobyov, 2015; Grady et al., 2003) rather than reflecting healthy age-dependent changes.

It is noteworthy that a recent study in the McGill-R-Thy1-APP rat model of AD reported that neuroimaging biomarkers used in clinical AD research are valid in this transgenic model as well, even without clear neuronal loss or tauopathy (Leon et al., 2010; Parent et al., 2017). For example, they report early abnormal FC and cognitive deficits at 9–11 months of age prior to hypometabolism and Aβ detected by PET imaging at 16–19 months of age. Additionally, progressive cognitive deficits as well as reduced hippocampal volume and CSF $A\beta_{1-42}$ were described (Parent et al., 2017). Together, these results seem to indicate that mainly the amyloid-driven synaptotoxic effects leads to a biomarker profile highly analogous of human AD. Nevertheless, although initial synaptic vulnerability to amyloid toxicity might kick-start the disconnection cascade, the influence of consequent tauopathy cannot be ignored, especially when assessing potential therapeutic strategies. Therefore, the TgF344-AD rat model might be a better alternative to be used in future translational studies as this model also entails tauopathy as well as neuronal loss (Cohen et al., 2013). Discrepancies in results between the McGill-R-Thy1-APP and TgF344-AD rat could be explained by differences in experimental design, such as time points investigated but also use of anaesthesia. Whereas no early hyperconnectivity nor clear macroscopic volume loss was detected in the TgF344-AD rat model using the techniques described here, it is possible that these effects occurred outside the scope of this study, so future studies might examine the TgF344-AD rat model at both younger and older ages.

5. Conclusion

We have shown that striking FC dysfunction was the earliest detectable hallmark in the TgF344-AD rat model and that this preceded the presence of structural changes as assessed using the current methodology. Overall, the progressive aggravation of neuroimaging abnormalities, as well as the regions affected in the TgF344-AD rat model are in line with previous human AD research, which show pathological changes in posterior cingulate cortex, hippocampal areas and temporal lobes. Importantly, FC deficits were detected prior to significant amyloid plaque deposition, supporting the use of rsfMRI as an early non-

invasive MRI marker reflecting underlying early-stage synaptic or neuronal dysfunction. The characterization of AD pathology in this rat model using highly translational MRI techniques highlights the potential of this model to be used in valuable future preclinical AD research.

Acknowledgements

This research was supported by the European Union's Seventh Framework Programme (FP7/2007-2013) under grant agreement number HEALTH-F2-2011-278850 (INMiND) and by the Fund for Scientific Research Flanders (FWO) (grant agreements G067515N and G057615N). The purchase of the TgF344-AD rat was jointly supported by the European Union's Seventh Framework Programme (FP7/2007-2013) under grant agreement n° HEALTH-F2-2011-278850 (INMiND) and Alzheimer Research UK network funds. The Bruker Pharmascan 7T system (Bruker, Ettlingen, Germany) was funded through the Hercules Foundation Belgium (Grant Nr. AUHA/012) and in part by the Flemish Impulse funding for heavy scientific equipment (42/FA010100/123) granted to Prof. Dr. Annemie Van der Linden. The computational resources and services used in this work were provided by the HPC core facility CalcUA of the Universiteit Antwerpen, the VSC (Flemish Supercomputer Center), funded by the Hercules Foundation and the Flemish Government – department EWI. This research was further supported by the grants D-17/02/006-SUM and E-15/22/113-COS from the Paracelsus Medical University Research Fund PMU-FFF.

Appendix A. Supplementary data

Supplementary data to this article can be found online at https://doi.org/10.1016/j.nbd.2018.11.010.

References

Adamczak, J., et al., 2017. Neurogenesis upregulation on the healthy hemisphere after stroke enhances compensation for age-dependent decrease of basal neurogenesis. Neurobiol. Dis. 99, 47–57.
Arenaza-Urquijo, E.M., et al., 2013. Relationships between years of education and gray matter volume, metabolism and functional connectivity in healthy elders. NeuroImage 83, 450–457.
Ashburner, J.R., 2015. Tensor-based morphometry. In: Toga, A.W. (Ed.), Brain Mapping. Academic Press, Waltham, pp. 383–394.
Ashburner, J., Ridgway, G.R., 2012. Symmetric diffeomorphic modeling of longitudinal structural MRI. Front. Neurosci. 6, 197.
Badhwar, A., et al., 2017. Resting-state network dysfunction in Alzheimer's disease: a systematic review and meta-analysis. Alzheimers Dement (Amst). 8, 73–85.
Balachandar, R., et al., 2015. A study of structural and functional connectivity in early Alzheimer's disease using rest fMRI and diffusion tensor imaging. Int. J. Geriatr. Psychiatry. 30, 497–504.
Barage, S.H., Sonawane, K.D., 2015. Amyloid cascade hypothesis: Pathogenesis and therapeutic strategies in Alzheimer's disease. Neuropeptides 52, 1–18.
Bazzigaluppi, P., et al., 2018 Mar. Early-stage attenuation of phase-amplitude coupling in the hippocampus and medial prefrontal cortex in a transgenic rat model of Alzheimer's disease. J. Neurochem. 144 (5), 669–679.
Bobkova, N., Vorobyov, V., 2015. The brain compensatory mechanisms and Alzheimer's disease progression: a new protective strategy. Neural Regen. Res. 10, 696–697.
Braak, H., Braak, E., 1991. Neuropathological stageing of Alzheimer-related changes. Acta Neuropathol. 82, 239–259.
Braak, H., Braak, E., 1995. Staging of Alzheimer's disease-related neurofibrillary changes. Neurobiol. Aging 16, 271–278 (discussion 278-84).
Brun, A., Englund, E., 1986. A white matter disorder in dementia of the Alzheimer type: a pathoanatomical study. Ann. Neurol. 19, 253–262.
Busche, M.A., et al., 2012. Critical role of soluble amyloid-beta for early hippocampal hyperactivity in a mouse model of Alzheimer's disease. Proc. Natl. Acad. Sci. U. S. A. 109, 8740–8745.
Chase, A., 2014. Alzheimer disease: Altered functional connectivity in preclinical dementia. Nat. Rev. Neurol. 10, 609.
Cohen, R.M., et al., 2013. A transgenic Alzheimer rat with plaques, tau pathology, behavioral impairment, oligomeric abeta, and frank neuronal loss. J. Neurosci. 33, 6245–6256.
Daianu, M., et al., 2015. Multi-Shell Hybrid Diffusion Imaging (HYDI) at 7 Tesla in TgF344-AD Transgenic Alzheimer Rats. PLoS One 10, e0145205.
Do Carmo, S., Cuello, A.C., 2013. Modeling Alzheimer's disease in transgenic rats. Mol. Neurodegener. 8, 37.
Dubois, B., et al., 2007. Research criteria for the diagnosis of Alzheimer's disease: revising the NINCDS-ADRDA criteria. Lancet Neurol. 6, 734–746.
Ewers, M., et al., 2011. Neuroimaging markers for the prediction and early diagnosis of Alzheimer's disease dementia. Trends Neurosci. 34, 430–442.
Gibbs, R.A., et al., 2004. Genome sequence of the Brown Norway rat yields insights into mammalian evolution. Nature 428, 493–521.
Gold, B.T., et al., 2012. White matter integrity and vulnerability to Alzheimer's disease: preliminary findings and future directions. Biochim. Biophys. Acta 1822, 416–422.
Gordon, J.A., 2011. Oscillations and hippocampal-prefrontal synchrony. Curr. Opin. Neurobiol. 21, 486–491.
Grady, C.L., et al., 2003. Evidence from functional neuroimaging of a compensatory prefrontal network in Alzheimer's disease. J. Neurosci. 23, 986–993.
Grandjean, J., et al., 2014a. Optimization of anesthesia protocol for resting-state fMRI in mice based on differential effects of anesthetics on functional connectivity patterns. NeuroImage 102 (Pt 2), 838–847.
Grandjean, J., et al., 2014b. Early alterations in functional connectivity and white matter structure in a transgenic mouse model of cerebral amyloidosis. J. Neurosci. 34, 13780–13789.
Hamaide, J., et al., 2017. Exploring sex differences in the adult zebra finch brain: in vivo diffusion tensor imaging and ex vivo super-resolution track density imaging. NeuroImage 146, 789–803.
Hardy, J.A., Higgins, G.A., 1992. Alzheimer's disease: the amyloid cascade hypothesis. Science 256, 184–185.
Hoozemans, J.J., et al., 2006. Neuroinflammation and regeneration in the early stages of Alzheimer's disease pathology. Int. J. Dev. Neurosci. 24, 157–165.
Jacob, H.J., Kwitek, A.E., 2002. Rat genetics: attaching physiology and pharmacology to the genome. Nat Rev Genet. 3, 33–42.
Johnson, K.A., et al., 2012. Brain imaging in Alzheimer disease. Cold Spring Harb. Perspect. Med. 2, a006213.
Jonckers, E., et al., 2011. Functional connectivity fMRI of the rodent brain: comparison of functional connectivity networks in rat and mouse. PLoS One 6, e18876.
Joo, I.L., et al., 2017. Early neurovascular dysfunction in a transgenic rat model of Alzheimer's disease. Sci. Rep. 7, 46427.
Leech, R., Sharp, D.J., 2014. The role of the posterior cingulate cortex in cognition and disease. Brain 137, 12–32.
Leon, W.C., et al., 2010. A novel transgenic rat model with a full Alzheimer's-like amyloid pathology displays pre-plaque intracellular amyloid-beta-associated cognitive impairment. J. Alzheimers Dis. 20, 113–126.
Mucke, L., Selkoe, D.J., 2012. Neurotoxicity of amyloid beta-protein: synaptic and network dysfunction. Cold Spring Harb Perspect Med. 2, a006338.
Munoz-Moreno, E., et al., 2018. Early brain connectivity alterations and cognitive impairment in a rat model of Alzheimer's disease. Alzheimers Res. Ther. 10, 16.
Nasrallah, F.A., et al., 2016. Functional connectivity MRI tracks memory networks after maze learning in rodents. NeuroImage 127, 196–202.
Nir, T.M., et al., 2013. Effectiveness of regional DTI measures in distinguishing Alzheimer's disease, MCI, and normal aging. Neuroimage Clin. 3, 180–195.
Paasonen, J., et al., 2018. Functional connectivity under six anesthesia protocols and the awake condition in rat brain. NeuroImage 172, 9–20.
Parent, M.J., et al., 2017. Multimodal Imaging in Rat Model Recapitulates Alzheimer's Disease Biomarkers Abnormalities. J. Neurosci. 37, 12263–12271.
Paxinos, G., Watson, C., 2007. The Rat Brain in Stereotaxic Coordinates. Academic Press.
Peca, S., et al., 2013. Neurovascular decoupling is associated with severity of cerebral amyloid angiopathy. Neurology 81, 1659–1665.
Pentkowski, N.S., et al., 2018. Anxiety-like behavior as an early endophenotype in the TgF344-AD rat model of Alzheimer's disease. Neurobiol. Aging 61, 169–176.
Princz-Kranz, F.L., et al., 2010. Vascular response to acetazolamide decreases as a function of age in the arcA beta mouse model of cerebral amyloidosis. Neurobiol. Dis. 40, 284–292.
Quiroz, Y.T., et al., 2015. Brain imaging and blood biomarker abnormalities in children with autosomal dominant Alzheimer Disease: a cross-sectional study. JAMA Neurol. 72, 912–919.
Rao, J.S., et al., 2012. Neuroinflammation and synaptic loss. Neurochem. Res. 37, 903–910.
Rorabaugh, J.M., et al., 2017. Chemogenetic locus coeruleus activation restores reversal learning in a rat model of Alzheimer's disease. Brain 140, 3023–3038.
Sampath, D., et al., 2017. Cognitive dysfunction in major depression and Alzheimer's disease is associated with hippocampal-prefrontal cortex dysconnectivity. Neuropsychiatr. Dis. Treat. 13, 1509–1519.
Schindelin, J., et al., 2012. Fiji: an open-source platform for biological-image analysis. Nat. Methods 9, 676–682.
Scholvinck, M.L., et al., 2010. Neural basis of global resting-state fMRI activity. Proc. Natl. Acad. Sci. U. S. A. 107, 10238–10243.
Selkoe, D.J., 2001. Alzheimer's disease: genes, proteins, and therapy. Physiol. Rev. 81, 741–766.
Selkoe, D.J., 2002. Alzheimer's disease is a synaptic failure. Science 298, 789–791.
Shah, D., et al., 2016a. Cholinergic and serotonergic modulations differentially affect large-scale functional networks in the mouse brain. Brain Struct. Funct. 221, 3067–3079.
Shah, D., et al., 2016b. Early pathologic amyloid induces hypersynchrony of BOLD resting-state networks in transgenic mice and provides an early therapeutic window before amyloid plaque deposition. Alzheimers Dement. 12, 964–976.
Shankar, G.M., et al., 2007. Natural oligomers of the Alzheimer amyloid-beta protein induce reversible synapse loss by modulating an NMDA-type glutamate receptor-dependent signaling pathway. J. Neurosci. 27, 2866–2875.
Sheline, Y.I., Raichle, M.E., 2013. Resting state functional connectivity in preclinical Alzheimer's disease. Biol. Psychiatry 74, 340–347.
Sigurdsson, T., Duvarci, S., 2015. Hippocampal-Prefrontal Interactions in Cognition, Behavior and Psychiatric Disease. Front. Syst. Neurosci. 9, 190.

Smith, L.A., McMahon, L.L., 2018. Deficits in synaptic function occur at medial perforant path-dentate granule cell synapses prior to Schaffer collateral-CA1 pyramidal cell synapses in the novel TgF344-Alzheimer's Disease Rat Model. Neurobiol. Dis. 110, 166–179.
Stebbins, G.T., Murphy, C.M., 2009. Diffusion tensor imaging in Alzheimer's disease and mild cognitive impairment. Behav. Neurol. 21, 39–49.
Thal, D.R., et al., 2002. Phases of a beta-deposition in the human brain and its relevance for the development of AD. Neurology 58, 1791–1800.
van den Heuvel, M.P., Hulshoff Pol, H.E., 2010. Exploring the brain network: a review on resting-state fMRI functional connectivity. Eur. Neuropsychopharmacol. 20, 519–534.
Voorhees, J.R., et al., 1 October 2018. (−)-P7C3-S243 protects a rat model of alzheimer's disease from neuropsychiatric deficits and neurodegeneration without altering amyloid deposition or reactive glia. Biol. Psychiatry 84 (7), 488–498.
Weaver, K.E., et al., 2016. Directional patterns of cross frequency phase and amplitude coupling within the resting state mimic patterns of fMRI functional connectivity. NeuroImage 128, 238–251.
Weston, P.S., et al., 2015. Diffusion imaging changes in grey matter in Alzheimer's disease: a potential marker of early neurodegeneration. Alzheimers Res. Ther. 7, 47.
Zhang, Y., et al., 2001. Segmentation of brain MR images through a hidden Markov random field model and the expectation-maximization algorithm. IEEE Trans. Med. Imaging 20, 45–57.